PAPER

A systematic study of LYSO:Ce, LuAG:Ce and GAGG:Ce scintillating fibers properties

Published by IOP Publishing for Sissa Medialab
Received: *August 4, 2021*
Accepted: *October 15, 2021*
Published: *November 8, 2021*

A systematic study of LYSO:Ce, LuAG:Ce and GAGG:Ce scintillating fibers properties

K. Rusiecka,[a,*] R. Hetzel,[b] J. Kasper,[b] M. Kazemi Kozani,[a] N. Kohlhase,[c] M. Kołodziej,[a] R. Lalik,[a] A. Magiera,[a] W. Migdał,[a] M. Rafecas,[c] A. Stahl,[b] V. Urbanevych,[a] M.L. Wong[a] and A. Wrońska[a]

[a] *M. Smoluchowski Institute of Physics, Jagiellonian University, Kraków, Poland*
[b] *Physics Institute III B, RWTH Aachen University, Aachen, Germany*
[c] *Institute of Medical Engineering, University of Lübeck, Lübeck, Germany*

E-mail: katarzyna.rusiecka@doctoral.uj.edu.pl

Abstract: Properties of different scintillating fibers were examined and compared, as a part of the design optimization of the SiFi-CC detector, currently under development for proton therapy monitoring. Three scintillating materials were considered as candidates to constitute the active part of the detector: LYSO:Ce, LuAG:Ce and GAGG:Ce. All investigated samples had an elongated, fiber-like shape and were read out on both ends using silicon photomultipliers (SiPMs). Samples of LYSO:Ce material provided by four different manufacturers were included in the survey. Additionally, different types of optical coupling media, wrapping and coating materials were investigated. The following properties of the scintillating fibers were determined: attenuation length, position-, energy-, timing resolution and light collection. Two models were used to describe the propagation of scintillating light in the fiber and quantify the light attenuation: exponential light attenuation model (ELA) and exponential light attenuation model with light reflection (ELAR). Energy and position reconstruction were also performed using the two above methods. It was shown, that the ELAR model performs better in terms of description of the light attenuation process. However, energy and position reconstruction results are comparable for the two proposed methods. Based on the results of measurements with scintillating fibers in different configurations we concluded that LYSO:Ce fibers wrapped in Al foil (bright side facing towards the fiber) provided the best trade-off between the energy- (8.56% at 511 keV) and position (32 mm) resolutions and thus will be the optimal choice for the SiFi-CC detector. Additionally, the study of different optical coupling media showed, that the silicone pads coupling ensures good stability of the system performance and parameters.

Keywords: Gamma detectors (scintillators, CZT, HPGe, HgI etc); Instrumentation for hadron therapy; Scintillators and scintillating fibres and light guides; Scintillators, scintillation and light emission processes (solid, gas and liquid scintillators)

*Corresponding author.

https://doi.org/10.1088/1748-0221/16/11/P11006

2021 JINST 16 P11006

Contents

2021 JINST 16 P11006

1 Introduction

Scintillators are a basis of many important detection systems, e.g. calorimeters used in large high-energy physics and nuclear physics experiments, medical imaging devices, homeland security or industrial control. Growing popularity of scintillating detectors has driven a demand for better performing materials and caused a rapid progress in the field over the last decades. It resulted in the development of many novel materials as well as deeper understanding of the processes occurring in the scintillators [1, 2]. Thanks to the available variety of scintillators and new techniques of production, it is possible to choose an optimal material for the desired application and even tune its properties with different doping or surface treatment. The focus of this study was to find the

best scintillator for a novel detection setup proposed by the SiFi-CC collaboration (**Si**PM and heavy scintillation **Fi**ber-based **C**ompton **C**amera).[1] SiFi-CC plans to enable on-line monitoring of the dose distribution delivered during proton therapy. The proposed setup can be operated in two modes: as a Compton camera or with a coded mask. In both cases, the active parts of the detector will consist of thin and elongated scintillating fibers. A detailed description of the proposed setup can be found in [3, 4]. The scintillating material for the active part of the detector needs to meet the following criteria:

- Large density and Z_{eff}— the principle of operation of the SiFi-CC system is based on the detection of a prompt-gamma radiation, a by-product of the proton therapy, with the focus on the 2–7 MeV energy range. Large density and Z_{eff} will increase the detection efficiency.
- Large light output — it is desired since it enhances the energy resolution. Compton camera operation relies on calculation of Compton scattering angles based on the energy deposits. Therefore, the energy resolution of the detector has a direct influence on the quality of the obtained images.
- Short decay constant — which allows the suppression of pile-up events. This is important especially when operating in a high radiation environment [4].
- Good time resolution — having a good time resolution of the order of 1 ns is required to build coincidences and suppress accidentals.
- Appropriate attenuation length — to register two correlated signals at both ends of the fiber, the selected scintillating material should be relatively transparent to its own scintillating light. However, large attenuation length results in poor position resolution. Therefore, the optimal attenuation length needs to be determined at which both energy and position can be reasonably reconstructed.
- Appropriate mechanical properties — mechanical properties of the scintillator should allow machining and cutting into the desired shape.
- No hygroscopicity — hygroscopic scintillating materials require a dedicated casing, which introduces additional dead space in the detector and makes material handling more complicated. This is particularly inconvenient in detectors consisting of many small scintillating elements.
- Low or nonexistent internal activity — many of the modern heavy scintillating materials contain rare earth elements. These elements usually have in their natural composition an admixture of radioactive isotopes. It results in an intrinsic activity which contributes to background.
- Scintillator emission spectrum matching the sensitivity range of the photodetector — to ensure high photon detection efficiency.
- Price and availability — those aspects are non-negligible for devices with commercialization potential.

[1] https://bragg.if.uj.edu.pl/sificc.

2021 JINST 16 P11006

Table 1. Properties of scintillating materials chosen for the study, as reported by producers or available research results.

	LuAG:Ce	LYSO:Ce[2]	GAGG:Ce
Formula	$Lu_3Al_5O_{12}$:Ce	$(Lu,Y)_2SiO_5$:Ce	$Gd_3Al_2Ga_3O_{12}$:Ce
Density [g cm^{-3}]	6.73	7.1–7.4	6.68
Z_{eff}	63	62–66	51
Refractive index (n)	1.84 @633 nm	1.82 @420 nm	1.9 @500 nm
Maximum of emission [nm]	535	420	520
Decay constant [ns]	70 + slow component	≤44	30 (25 %) 80 (60 %) 100–200 (15 %)
Photon yield [ph MeV^{-1}]	25×10^3	$(25–30) \times 10^3$	$(22–60) \times 10^3$
Attenuation length [mm]	50–320	~400	220–320
Radiation length at 511 keV [mm]	13	11.6	15.9
Energy resolution at 662 keV [%]	6.7	8–8.7	4.9–8.3
Internal activity [cps g^{-1}]	37	39	-
Producers of the investigated samples	Crytur	Epic Crystal, Meta Laser, Tianle, Shalom EO	Fomos Materials
References	[5–7]	[7–12]	[13–18]

2 Materials and methods

2.1 Scintillating materials

Based on the criteria listed in the previous section, the following scintillating materials were chosen as potential candidates for the active part of the SiFi-CC detector: LYSO:Ce, LuAG:Ce and GAGG:Ce. Table 1 summarizes the properties of those scintillators. Samples of selected materials were purchased from various vendors, as listed in the last but one row of table 1. All purchased fiber samples had an elongated, cuboid shape with a square 1×1 mm^2 cross section and a length of 100 mm. Examples of investigated scintillating fibers are shown in figure 1. Additionally, selected LYSO:Ce fibers were coated or wrapped in various materials in order to investigate the influence of surface modifications. The following types of wrappings and coatings prepared on site were tested: bright aluminum foil (bright side facing the fiber), mat aluminum foil (mat side facing the fiber), metalized Mylar foil, Teflon, light guide coating, black heat shrink, AlZn spray paint. In addition, the following samples of LYSO:Ce fibers wrapped by the producer were purchased: first wrapped in ESR reflector and aluminum foil, and the other painted with $BaSO_4$-based paint and wrapped in aluminum foil.

[2]Properties depend on the producer.

2021 JINST 16 P11006

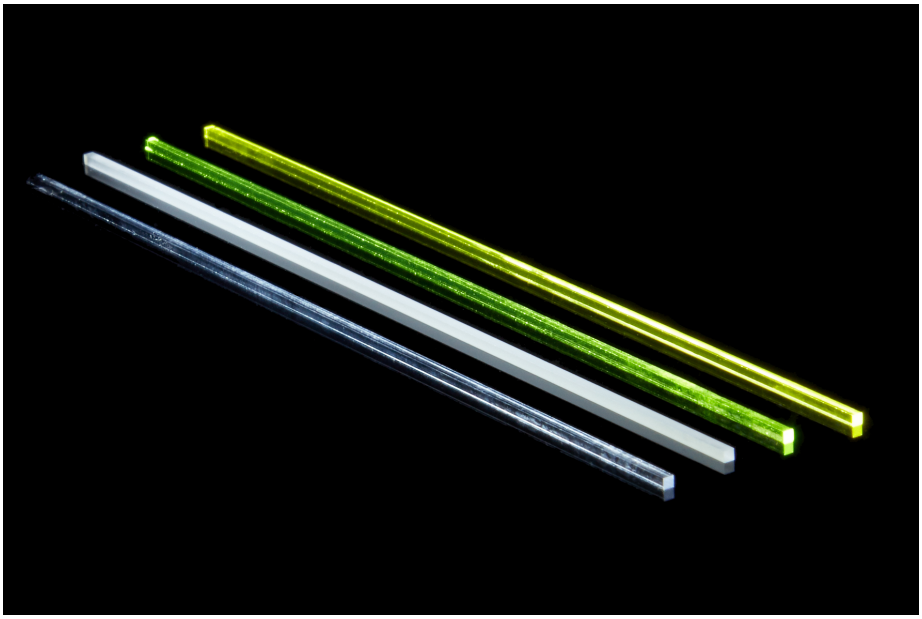

Figure 1. Samples of investigated scintillating fibers. From left: LYSO:Ce, LYSO:Ce (unpolished), LuAG:Ce, GAGG:Ce.

2.2 Experimental setup and data acquisition

To study the properties of scintillating fibers, a dedicated test bench was constructed as shown in figure 2. The entire setup was placed in a light-tight box. The investigated fiber was mounted in a holder and coupled at both ends to SensL SiPMs (C series, $3 \times 3\,\mathrm{mm}^2$, microcell size 20 µm) operated on custom boards [19]. The choice of the SiPMs was motivated by their relatively high photon detection efficiency for wavelengths between 420 nm and 530 nm, matching well the emission spectra of the investigated scintillation materials. The custom boards housing the SiPMs included a hardware temperature correction circuit which tuned the bias voltage to maintain constant gain with changing temperature. The non-linearity of the SiPMs response is negligible due to a large difference between the number of SiPMs microcells (10998) and the typical number of registered photoelectrons (200–250).

In order to ensure good optical contact between the SiPM and the investigated fiber, one of the following coupling media was used: Saint Gobain BC-630 silicone grease ($n_{\mathrm{gel}} = 1.47$, thickness $d_{\mathrm{gel}} \approx 0.4\,\mathrm{mm}$) or Eljen EJ-560 silicone rubber optical interface ($n_{\mathrm{pad}} = 1.43$, thickness $d_{\mathrm{pad}} = 1\,\mathrm{mm}$). Additional test measurements with no coupling medium were also performed ($n_{\mathrm{air}} = 1$, thickness $d_{\mathrm{air}} \approx 0.6\,\mathrm{mm}$). Moreover, the setup included a micrometer screw which allowed precise tightening of the fiber between the layers of coupling and SiPMs, ensuring stable and repetitive connections.

The setup featured an electronic collimator on a remotely controllable platform, inspired by Anfré et al. [20]. The reference detector in the collimator consisted of a SensL SiPM (C series, $3 \times 3\,\mathrm{mm}^2$, microcell size 20 µm) and a LYSO:Ce crystal ($2 \times 3 \times 20\,\mathrm{mm}^3$) attached to it. The ^{22}Na source was placed between the investigated fiber and the reference detector. The electronic collimator relies on two 511 keV photons emitted back-to-back as a result of positron annihilation in the ^{22}Na source. Such a collimation system allows for the irradiation of the investigated fiber at a desired

2021 JINST 16 P11006

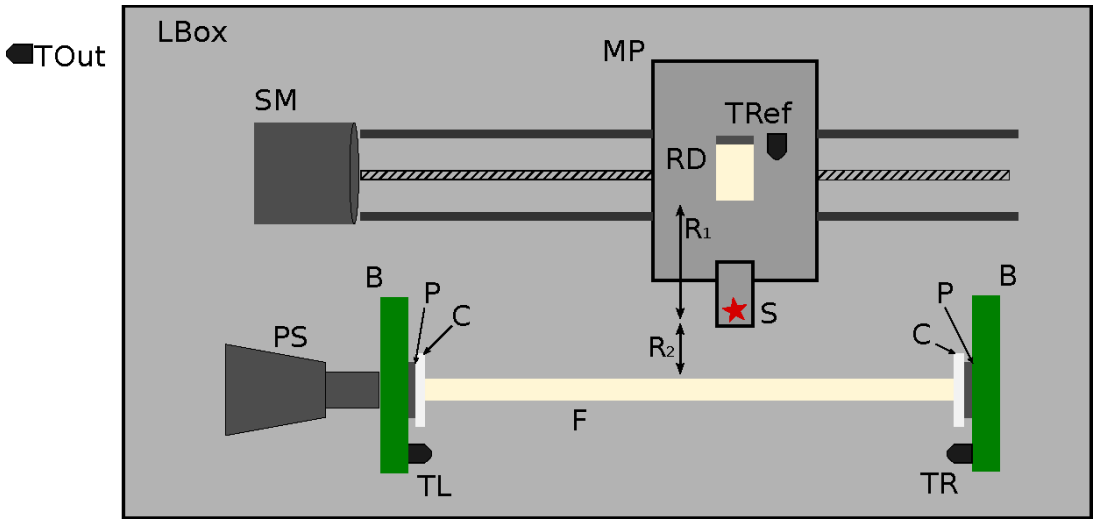

Figure 2. Scheme of the experimental setup (not to scale). Symbols in the picture denote: F — fiber, C — optical coupling, P — SiPM, B — PCB housing the SiPM, TR — temperature sensor (right), TL — temperature sensor (left), PS — positioning micrometer screw, S — radioactive source, RD — reference detector, TRef — temperature sensor for the reference detector, MP — moving platform for the electronic collimation system, SM — stepping motor, LBox — light-tight box, TOut — temperature sensor placed outside of the light-tight box, R_1 — distance between the radioactive source and the reference detector, R_2 — distance between the radioactive source and the investigated fiber.

position, with the position and area of irradiation determined by the geometry of the setup. In the presented experimental setup the distances R_1 and R_2 were respectively 10 mm and 5 mm, which resulted in a 1 mm irradiation window on the fiber. This was an improvement from a past setup that used a lead collimator [21], which allowed to suppress Compton continuum in the spectra.

A CAEN Desktop Digitizer DT5742 was used for data acquisition with a sampling frequency of 1 GHz and an acquisition window of 1024 samples. The acquisition was triggered externally by a triple coincidence of signals from both ends of the investigated fiber and from the reference detector. These filtered signals were stored on a disk and subsequently analyzed with custom ROOT-based analysis software [22]. Primarily, the analysis extracted the amplitude, integral (charge), start time t_0, time over threshold (TOT), baseline and its standard deviation. Time t_0 expresses time relative to the trigger, when the signal reaches the threshold value of 40 mV. The TOT is defined as the time between t_0 and time when the signal falling edge crosses the set threshold. For each signal, the baseline and standard deviation of the baseline were calculated individually, taking into account first 50 samples in the acquisition window. This enabled event-wise baseline subtraction, as well as filtering out signals contaminated from external sources.

2.3 Measurement procedure and list of runs

Each fiber was examined individually. The experimental sequence was organized into series. Each series consisted of the registration of gamma spectra for different positions of ^{22}Na source along the fiber (position 0 mm corresponded to the left end of the fiber and position 100 mm to the right end). Extra precautions were taken to control measurement stability and experimental conditions.

2021 JINST 16 P11006

Every other measurement was recorded at a central position 50 mm in order to test the gain stability. Additionally, four independent temperature sensors were placed in the test bench. Temperature readings along with the monitoring measurements confirmed good performance of the hardware temperature correction of the SiPMs ensuring gain stability better than 1 %. Each fiber was examined twice, in two opposite orientations to observe possible effects stemming from differences in the coupling at fiber ends.

In total 64 measurement series were recorded in various conditions. Table 2 presents the list of analyzed series along with the experimental conditions. Collected data allowed to compare different scintillating materials, different vendors, types of SiPM-fiber coupling and wrapping or coating of the scintillating fibers.

Table 2. Summary of conducted measurements. The measurement series IDs are used hereafter in the figures. Numbers in bold denote the total number of series taken in the same conditions.

Material	Producer	Coupling	Coating/ wrapping	Measurement series
LYSO:Ce	Epic Crystal	Silicone pads	-	117, 119, 121, 123 **(4)**
LYSO:Ce	Meta Laser	Silicone pads	-	109, 111, 125, 127, 129, 131, 133, 135, 137, 139, 141, 143 **(12)**
LYSO:Ce	Shalom	Silicone pads	-	113, 115 **(2)**
LYSO:Ce	Tianle	Silicone pads	-	98, 100, 102, 104, 106, 201, 203, 229 **(8)**
GAGG:Ce	Fomos	Silicone pads	-	181, 183, 185, 187 **(4)**
LuAG:Ce	Crytur	Silicone pads	-	189, 191, 193, 195 **(4)**
LYSO:Ce	Tianle	Silicone gel	-	225, 227 **(2)**
LYSO:Ce	Tianle	Air gaps	-	205, 207 **(2)**
LYSO:Ce	Meta Laser/ Shalom	Silicone pads	Teflon	145, 147, 149, 151, 153, 155 **(6)**
LYSO:Ce	Meta Laser	Silicone pads	Mylar	165, 167, 169, 171 **(4)**
LYSO:Ce	Epic Crystal/ Meta Laser	Silicone pads	Al (mat)	157, 159, 161, 163 **(4)**
LYSO:Ce	Epic Crystal/ Meta Laser	Silicone pads	Al (bright)	173, 175, 177, 179 **(4)**
LYSO:Ce	Tianle	Silicone pads	Light guide coating	209, 211 **(2)**
LYSO:Ce	Meta Laser/ Shalom	Silicone pads	Heat shrink	219, 221 **(2)**
LYSO:Ce	Shalom	Silicone pads	ESR + Al	231, 233 **(2)**
LYSO:Ce	Shalom	Silicone pads	White paint + Al	235, 237, 239, 241 **(4)**

2021 JINST 16 P11006

2.4 Data preprocessing

The charge spectra were calibrated to photoelectrons (PE). The 511 keV peak and the surrounding background were parameterized using the following fit function:

$$f(x) = c \cdot \exp\left(-\frac{(x-\mu)^2}{2\sigma^2}\right) + p_1 \cdot \exp\left((x-p_2)\cdot p_3\right) + p_4, \tag{2.1}$$

where parameters of the Gaussian function describe the 511 keV peak: c — intensity, μ — mean charge (energy), σ — width, and parameters p_1–p_4 describe the background. Examples of charge spectra recorded at both ends of the fiber and at two different positions of the radioactive source can be seen in figure 3, where also the signal-background decomposition according to eq. (2.1) is shown. It can be observed that depending on the source position along the fiber the charge spectra change their shape and the 511 keV peak shifts as expected: towards larger charges for smaller source-SiPM distances. This is a consequence of the attenuation of the scintillation light in the fiber and so the charge spectra from both ends are expected to overlap when the source is at the central position of 50 mm. However, there were observed differences, like in figure 3, which we associate with differences in the coupling.

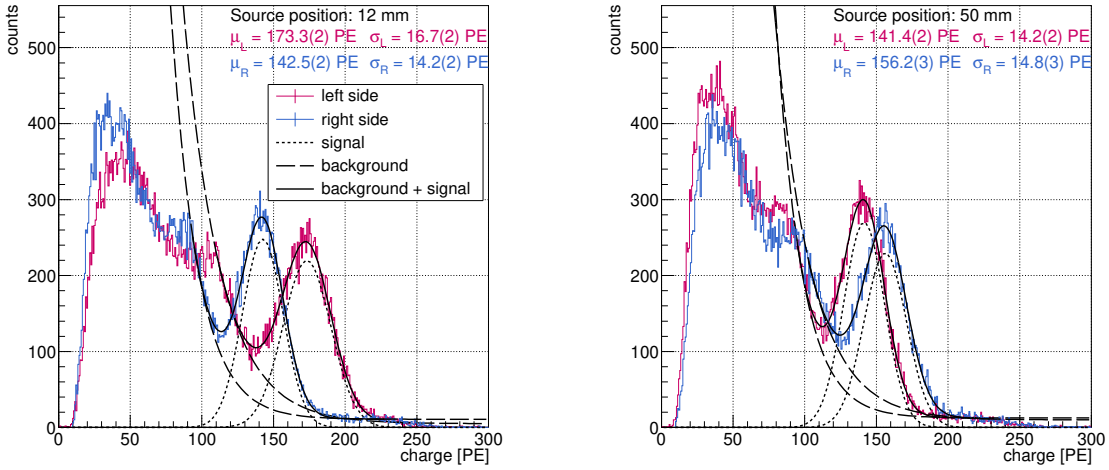

Figure 3. Examples of charge spectra recorded at both ends of the investigated LYSO:Ce fiber (series 109) and for two different source positions: 12 mm (left) and 50 mm (right). Each spectrum was described by a fit of eq. (2.1) — the resulting parameters of the 511 keV peaks are listed in each panel.

The charge and time spectra from the measurements were further analysed to obtain evaluation metrics such as attenuation length, energy-, time- and position resolution and light collection.

3 Light propagation models

3.1 Exponential light attenuation model (ELA)

Scintillating light produced during the interaction of ionizing radiation with the scintillating material is emitted isotropically. It is attenuated as it propagates through the scintillator. The

2021 JINST 16 P11006

most straightforward approach to describe scintillating light propagation in the scintillator assumes exponential attenuation [23, 24], where the parameter λ represents the attenuation length i.e. the distance into the material where the intensity of scintillating light drops by a factor of e. According to this exponential attenuation model, signals recorded at the left $S_l(x)$ and the right end $S_r(x)$ of the investigated fiber can be expressed as follows:

$$\begin{cases} S_l(x) = \xi_l S_0 \exp\left(\frac{-x}{\lambda}\right) \\ S_r(x) = \xi_r S_0 \exp\left(\frac{-(L-x)}{\lambda}\right) \end{cases} \tag{3.1}$$

where x stands for the position of the interaction, L is the total length of the fiber, S_0 is the intensity of the signal at the point of interaction, ξ_l and ξ_r are the light transmission factors associated with the coupling quality at the corresponding fiber ends. It needs to be noted that it is impossible to resolve the values of S_0 and ξ_i based on the experimental data, which is sensitive solely to their product. In eq. (3.1) it is assumed that the investigated fiber has homogeneous structure with no defects or doping gradient and light propagates alike in all directions. In such a situation light attenuation is direction-independent and can be described with a single λ parameter for both fiber ends. To determine the attenuation length of the investigated fiber, a dependence of the 511 keV peak position $\mu_{511\,\mathrm{keV}}$ on the source position was plotted for both fiber sides. Subsequently, eqs. (3.1) were simultaneously fitted to the two data sets to obtain single set of parameters (figure 4 left).

It can be observed in figure 4 (left) that the quality of the ELA fit is not satisfactory ($\chi^2/ndf = 56.59$). The description can be simplified using the quantity M_{LR}, which combines the signals recorded at both ends of the fiber [6]:

$$M_{\mathrm{LR}}(x) = \ln\left(\sqrt{\frac{S_r(x)}{S_l(x)}}\right), \tag{3.2}$$

The M_{LR} quantity is calculated event-by-event. The resulting M_{LR} distributions are described with the Gaussian function, with the mean depending linearly on the position of the interaction x. From eq. (3.1) and eq. (3.2) the slope a and offset b of that dependence can be derived:

$$\begin{cases} a = \frac{1}{\lambda} \\ b = -\frac{L/2}{\lambda} + \ln\left(\sqrt{\frac{\xi_r}{\xi_l}}\right). \end{cases} \tag{3.3}$$

Thus, a linear fit of the M_{LR}(x) dependence allows to determine the attenuation length of the investigated scintillating fiber (see figure 4, right).

Figure 4 shows a comparison of the ELA (left) and M_{LR} (right) methods for the same experimental series. Based on the χ^2/ndf values for both approaches it can be stated that the quality of the M_{LR} fit is better ($\chi^2/ndf = 1.43$), which may result from the fact that in the M_{LR} ratio some nonexponential components cancel. At the same time, the obtained attenuation length values are similar and agree within 3σ.

3.2 Exponential light attenuation model with light reflection (ELAR)

The poor quality of the fit presented in figure 4 (left) suggests that the simple exponential model does not describe accurately the light attenuation in thin scintillating fibers. Therefore we tested the

2021 JINST 16 P11006

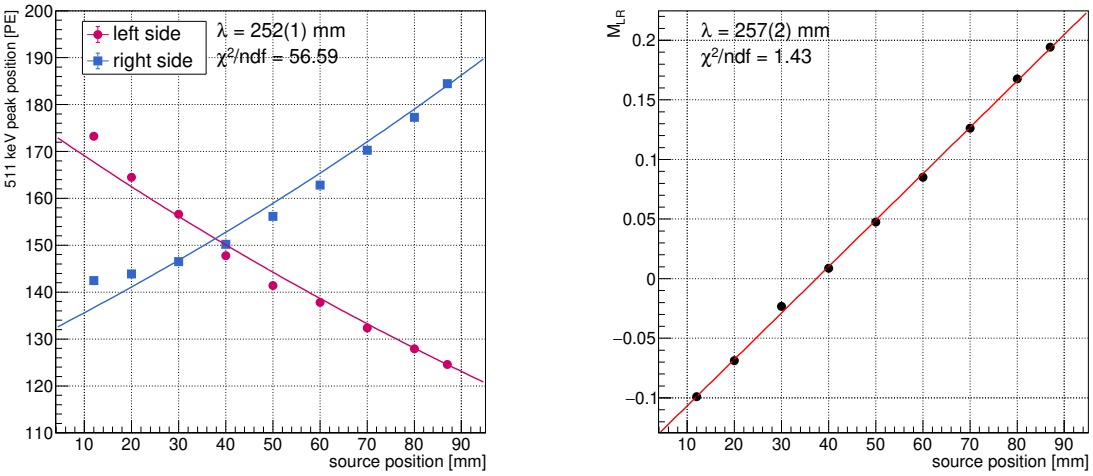

Figure 4. Left: example of ELA model fitted to the experimental points. Right: corresponding example of the M_{LR}(x) dependence along with a linear fit. Determined values of attenuation length (λ) and χ^2/ndf are listed for both approaches. Presented data comes from the series 109.

exponential attenuation model with light reflection (ELAR) motivated by the works [24] and [25]. In this model it is assumed that part of the scintillating light is reflected at the end of the fiber and subsequently propagates back to be registered at the opposite side. A simplified scheme of light propagation according to ELAR is depicted in figure 5. In that case the signal registered at the end

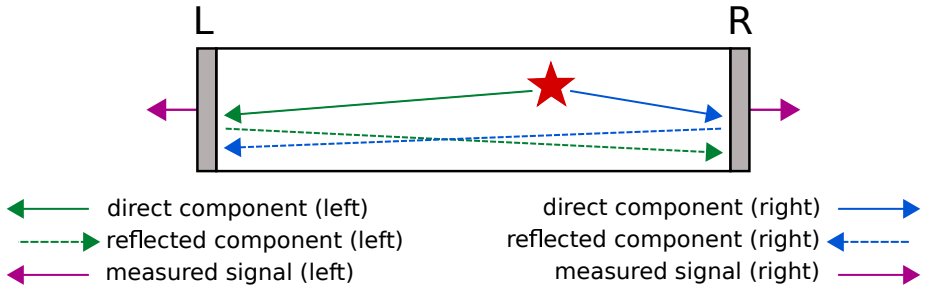

Figure 5. Simplified scheme of light propagation in the scintillating fiber according to the ELAR. A star represents the interaction point.

L (left) stems from the light emitted in the direction of this side (direct component) and from a fraction of light emitted towards the side R (right) which underwent reflection (reflected component). Direct components $P_l(x)$ and $P_r(x)$ emitted towards both ends of the investigated fiber are defined as follows:

$$\begin{cases} P_l(x) = S_0 \exp\left(\frac{-x}{\lambda}\right) \\ P_r(x) = S_0 \exp\left(\frac{-(L-x)}{\lambda}\right). \end{cases} \tag{3.4}$$

2021 JINST 16 P11006

Reflected components $R_l(x)$ and $R_r(x)$ registered at both ends can be written as:

$$\begin{cases} R_l(x) = \eta_r P_r(x) \exp\left(\frac{-L}{\lambda}\right) \\ R_r(x) = \eta_l P_l(x) \exp\left(\frac{-L}{\lambda}\right), \end{cases} \tag{3.5}$$

The η_i parameters are related to the light reflection at side i, however, their interpretation is not straightforward, since they include effects stemming from the geometry of the fiber and material properties. The total signals $S_l(x)$ and $S_r(x)$ are sums of the corresponding direct and reflected components, assuming no additional light losses, i.e. the fractions of corresponding primary and reflected components sum up to unity:

$$\begin{cases} S_l(x) = \xi_l S_0 \left[(1-\eta_l)\exp\left(\frac{-x}{\lambda}\right) + \eta_r \exp\left(\frac{-2L+x}{\lambda}\right)\right] \\ S_r(x) = \xi_r S_0 \left[(1-\eta_r)\exp\left(\frac{-L+x}{\lambda}\right) + \eta_l \exp\left(\frac{-L-x}{\lambda}\right)\right]. \end{cases} \tag{3.6}$$

Similarly as in the ELA model, it is not possible to resolve S_0 and ξ_i values in the fit of the experimental data. Therefore, the following parameterization was introduced to remove the ambiguity and reduce the number of parameters:

$$\begin{cases} \eta_r' = \frac{\eta_r}{1-\eta_l} \\ \eta_l' = \frac{\eta_l}{1-\eta_r}, \end{cases} \qquad \begin{cases} S_0' = \xi_l S_0 (1-\eta_l) \\ \xi = \frac{\xi_r (1-\eta_r)}{\xi_l (1-\eta_l)}. \end{cases} \tag{3.7}$$

Then, the total signals are the following:

$$\begin{cases} S_l(x) = S_0' \left[\exp\left(\frac{-x}{\lambda}\right) + \eta_r' \exp\left(\frac{-2L+x}{\lambda}\right)\right] \\ S_r(x) = \xi S_0' \left[\exp\left(\frac{-L+x}{\lambda}\right) + \eta_l' \exp\left(\frac{-L-x}{\lambda}\right)\right]. \end{cases} \tag{3.8}$$

In such a representation the coefficient ξ accounts for the possible asymmetry in light transmission in optical coupling. Values of that parameter obtained during data analysis range from 0.81 to 1.39. Values of effective η_i' parameters obtained in the data analysis range from 0.02 to 1.15.

The ELAR model allows not only to determine the attenuation length λ but also to reconstruct the direct light component based on the measured signal as follows:

$$\begin{cases} P_l^*(S_l, S_r) = \frac{\exp\left(\frac{L}{\lambda}\right)\left(\exp\left(\frac{L}{\lambda}\right)\xi S_l - S_r \eta_r'\right)}{\xi\left(\exp\left(\frac{2L}{\lambda}\right) - \eta_l' \eta_r'\right)} \\ \\ P_r^*(S_l, S_r) = -\frac{\exp\left(\frac{L}{\lambda}\right)\left(-\exp\left(\frac{L}{\lambda}\right) S_r + \xi S_l \eta_l'\right)}{\xi\left(\exp\left(\frac{2L}{\lambda}\right) - \eta_r' \eta_l'\right)}. \end{cases} \tag{3.9}$$

Thus, for the reconstruction of those direct components, one needs to first find the parameters of eq. (3.8) by a fit to the experimental data. Uncertainties of the reconstructed direct components were estimated taking into account contribution from the model fit as well as the experimental data as follows:

$$\sigma_{P_i^*} = \sqrt{\sigma^2_{f\,P_i^*} + \left(\frac{\partial P_i^*(S_l, S_r)}{\partial S_l}\sigma_{S_l}\right)^2 + \left(\frac{\partial P_i^*(S_l, S_r)}{\partial S_r}\sigma_{S_r}\right)^2}, \tag{3.10}$$

where $\sigma^2_{f\,P_i^*}$ represents variance of P_i^* and can be calculated with the matrix expression for error propagation [26]:

$$\sigma^2_{f\,P_i^*} = \mathbf{g}^{\mathrm{T}} \mathbf{V} \mathbf{g} \tag{3.11}$$

2021 JINST 16 P11006

where **V** is a covariance matrix of the fitted parameters and **g** is a vector containing partial derivatives of P_i^* with respect to its parameters. Results of the ELAR fit revealed correlations of some of the parameters, therefore the full formula including also non-diagonal matrix elements was used.

Example of the ELAR fit to the experimental data is shown in figure 6. The same set of the experimental points as in section 3.1 is presented here to compare the quality of the data description. Similarly as for the ELA fit eqs. (3.8) were fitted simultaneously to both data sets. Additionally, the attenuation curves were decomposed into direct and reflected components. Experimental points were also used to reconstruct the direct light component at every position of the source. Parameters of the fit along with the χ^2/ndf are listed. It can be observed that the proposed ELAR model accounting for the light reflection inside the fiber describes the experimental data better ($\chi^2/ndf = 5.07$) than the simple exponential model (ELA). Additionally, the reconstructed direct components reach the same intensity in the middle of the investigated fiber as expected, meaning that the model allows to correct for possible differences in coupling at the fiber ends.

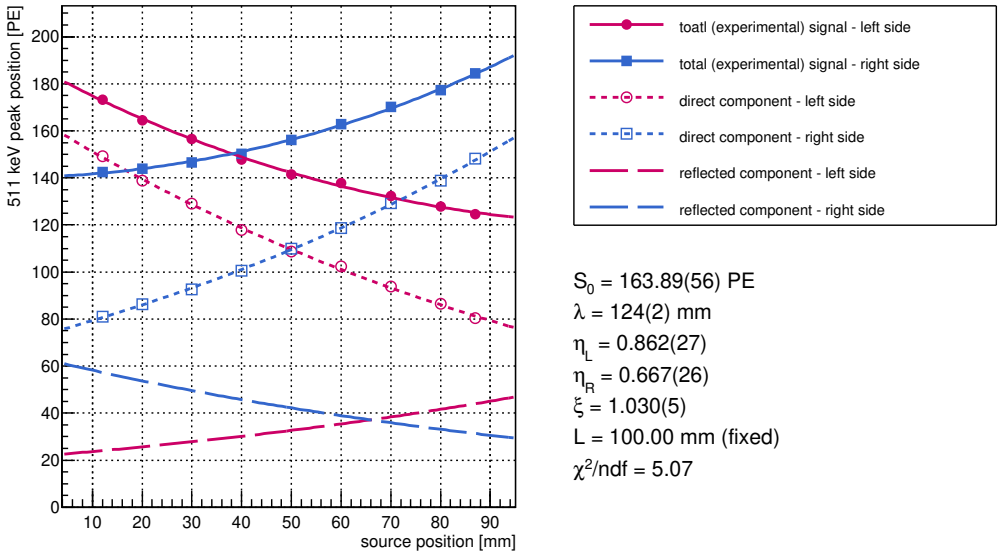

Figure 6. Example of ELAR fitted to the experimental points (filled symbols). Attenuation curves were additionally decomposed into direct and reflected components. Based on the experimental data and fit results, the direct components for both sides of the investigated fiber were reconstructed (empty symbols). Presented data comes from the series 109.

4 Scintillating fibers characteristics

4.1 Quality of data description by models

All three approaches of the light attenuation analysis: ELA, M_{LR} and ELAR were applied to the experimental data. In order to evaluate the performance of the models, the values of χ^2/ndf for each method were plotted for all experimental series (see figure 7). It can be observed that the M_{LR} method shows the best performance with the lowest χ^2/ndf values for most of the analyzed

2021 JINST 16 P11006

series (0.65–23.55). The ELAR method shows slightly worse performance, with somewhat higher or comparable values of χ^2/ndf (1.64–36.65). In most cases, the ELA model shows the worst performance, with the χ^2/ndf values ranging from 2.39 to 180.54. This comparison hints towards the M_{LR} and ELAR models as the more reliable for the determination of the attenuation length for the investigated scintillating fibers.

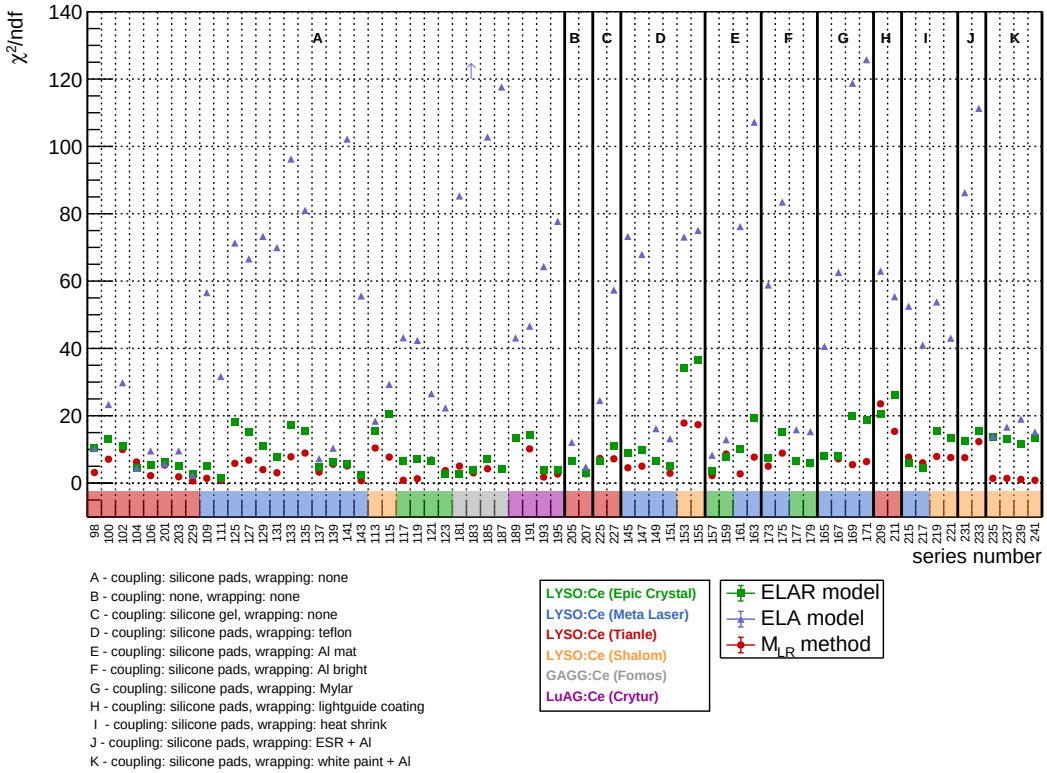

Figure 7. Reduced χ^2 values of ELA, ELAR and M_{LR} models fitting for all analyzed measurements. Value of χ^2/ndf of ELA fit for series 183 was too large to be shown in the graph and was denoted with an arrow. Value of χ^2/ndf for this series is 180.54.

4.2 Attenuation length

The values of attenuation length obtained using the three approaches (ELA, M_{LR} implementation of the ELA model and ELAR) were plotted for all analyzed experimental series (see figure 8). It can be observed that the results obtained with the ELA and M_{LR} methods are in agreement. At the same time, the values obtained with the ELAR method are significantly smaller for most of the analyzed experimental series. This is a consequence of the different light propagation pattern assumed in this model. Thus, the values should only be used together with the formalism of the model within which they were obtained and should be treated as effective attenuation length, valid within that model.

It can be seen in figure 8, that results of the ELAR model for Tianle fibers in groups A and B are inconclusive. Obtained values are unusually large for the investigated scintillator ($\lambda = 420$ mm reported in [12]), differ strongly from other investigated samples and have very large uncertainties. Additionally, results obtained for series 205 and 207 suggest that the limit of 10^4 imposed on the

2021 JINST 16 P11006

parameter value was reached in the fit. The fact, those inconclusive results were obtained only for the Tianle fibers in specific experimental conditions may suggest, that failure of the ELAR model is caused by some of the features of the fibers. It needs to be noted, that Tianle fibers, especially when no coupling is applied, are characterized by the largest attenuation length. Additionally, as can be seen in figure 7, for those series the performance of the ELA method is satisfactory. Therefore, it appears that the proposed ELAR model does not perform well since it introduces additional degrees of freedom, which are not required for a satisfactory description of data. Therefore, in further comparisons the results obtained with the use of ELAR model for Tianle fibers in groups A and B are disregarded.

Differences in attenuation length, which are in particular visible for different couplings and some of the wrappings and coatings, are further discussed in section 5.

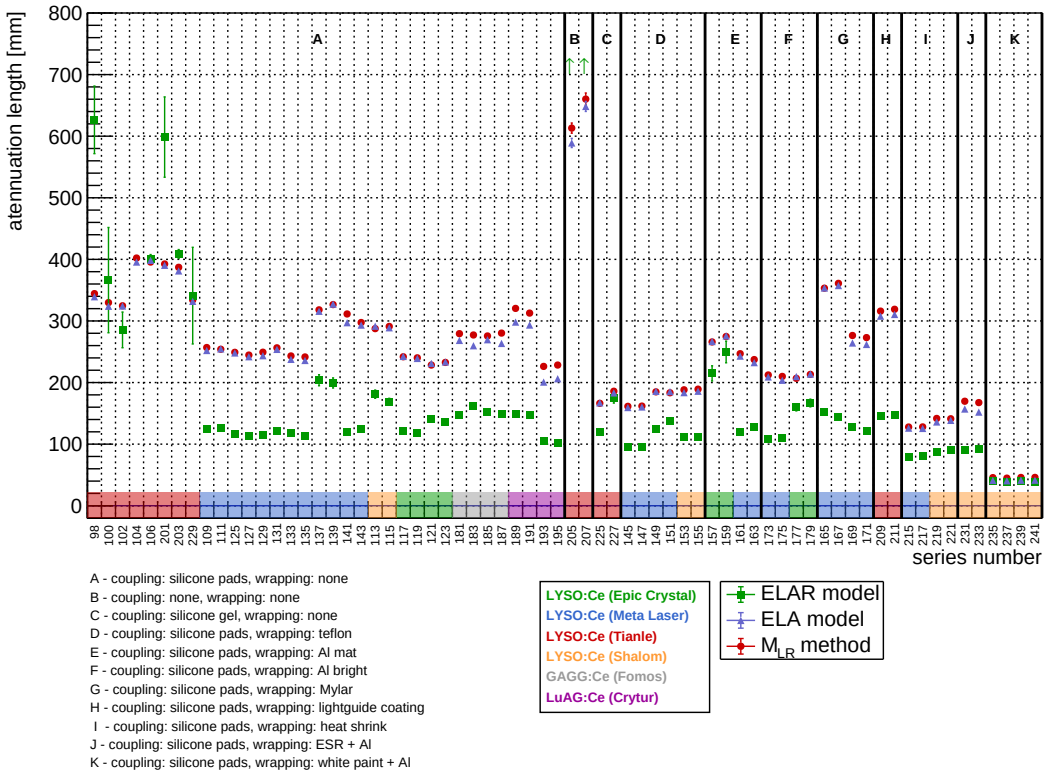

Figure 8. Values of attenuation length determined with the ELA, ELAR and M_{LR} methods for all analyzed experimental series. Attenuation lengths determined with the ELAR model for series 205 and 207 were too large to fit in the graph and were denoted with arrows. Values of attenuation length for those series are close to the imposed limit (10^4) with uncertainties close to 100 %.

4.3 Position reconstruction

Determination of the interaction point in the scintillating fiber is crucial for the performance of the SiFi-CC detector. The hit position can be reconstructed based either on the time difference between the correlated signals registered at both ends of the elongated detector, or the charge ratio of such signals. In case of the investigated scintillating fibers, the timing resolution turned out to be insufficient to perform position reconstruction using the first method (see section 4.5). Therefore,

2021 JINST 16 P11006

the method based on the charge ratio was used. For that reason the dependence of source position on M_{LR} (see eq. (3.2)) was parametrized with a linear function to serve as a calibration curve. Positions of interactions were reconstructed event-by-event and the obtained position spectrum was used to extract the source position in the measurement and the position resolution (defined as FWHM). The spectrum of residuals $X_{\mathrm{reco}} - X_{\mathrm{real}}$ for all source positions was additionally investigated, yielding the integrated position resolution for the examined fiber.

Taking advantage of the exponential attenuation model accounting for light reflection (ELAR), the second method of position reconstruction was proposed. In this method, the experimental data was recalculated using eq. (3.9) and the quantity M^*_{LR} was defined as follows:

$$M^*_{\mathrm{LR}} = \ln\left(\sqrt{\frac{P^*_r(S_l, S_r)}{P^*_l(S_l, S_r)}}\right), \tag{4.1}$$

i.e. as the ratio of direct light reaching the ends of the fiber, thus a linear behaviour of this quantity with position along the fiber is expected. In this model, position was reconstructed based on M^*_{LR}, otherwise the procedure was the same as above.

Figure 9 presents the results of the position reconstruction with the two methods for a chosen experimental series. The dependence of the residuals $X_{\mathrm{reco}} - X_{\mathrm{real}}$ on the source position (X_{real}) shows that both methods are equivalent as regards the position resolution.

Values of the position resolution determined with the two methods were plotted for all analyzed experimental series (see figure 10). Differences which can be observed for various materials, producers, couplings and wrappings are further discussed in section 5. It needs to be noted, that the position resolution is connected with the attenuation length of the investigated fiber, i.e. the fiber characterized with the large attenuation length will also have large position resolution. Therefore, the pattern of figure 8 is reproduced in that figure. Moreover, it can be seen that the two methods yield a similar position resolution for each analyzed series.

4.4 Energy reconstruction

Energy calibration of a single-channel response is not straightforward, since — as shown in section 2.4 — the obtained charge spectra are position-dependent. In the ELA model, this is eliminated by using a geometric mean of signals at both ends of the fiber $Q_{\mathrm{av}} = \sqrt{S_{\mathrm{l}}(x)S_{\mathrm{r}}(x)}$ which is position-independent [27]. Then, the energy can be reconstructed based on the measured charges using the following formula:

$$E(x) = \alpha \cdot \sqrt{S_l(x)S_r(x)} \tag{4.2}$$

where α is a calibration factor calculated for the reference energy $E_{\mathrm{ref}} = 511\,\mathrm{keV}$:

$$\alpha = \frac{E_{\mathrm{ref}}}{\sqrt{\mu_{l\,E_{\mathrm{ref}}}\mu_{r\,E_{\mathrm{ref}}}}}, \tag{4.3}$$

where $\mu_{i\,E_{\mathrm{ref}}}$ is the mean position of the peak corresponding to the reference energy in the charge spectrum at the i-th end of the fiber for a chosen source position. Using formulae (4.2) and (4.3), the energy reconstruction was performed event-by-event for all measurements in the series. An overall spectrum of all reconstructed energies in the whole series was additionally created to determine the energy resolution integrated over the fiber length.

2021 JINST 16 P11006

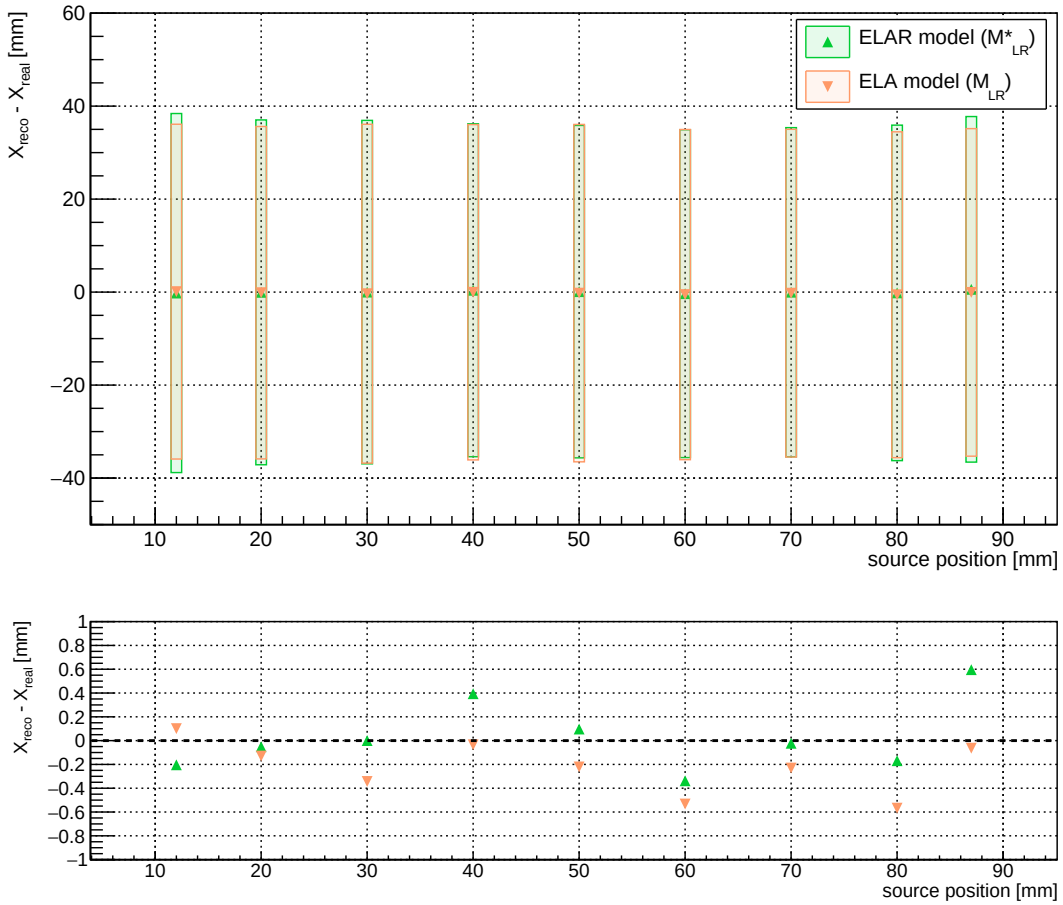

Figure 9. Top: difference between the real and reconstructed source positions. Results obtained using M_{LR} are plotted in orange, those of the ELAR model (using M^*_{LR}) in green. Error bars correspond to the resulting position resolution (FWHM). Bottom: same as above, but devoid of error bars and zoomed in to the y-axis range from −1 mm to 1 mm for better illustration of reconstruction residuals. Presented data comes from the series 109.

Similarly as for the position reconstruction, the energy reconstruction procedure was also carried out using the ELAR model, according to the modified equations:

$$E^* = \alpha^* \sqrt{P^*_l(S_l, S_r) P^*_r(S_l, S_r)}. \tag{4.4}$$

The coefficient α^* is defined analogously to the eq. (4.3). Examples of such summed spectra of reconstructed energy for a chosen LYSO:Ce fiber can be seen in figure 11: left — for the ELAR method and right — for the ELA method. The spectra were fitted with the eq. (2.1) in order to determine the energy resolution (calculated as $ER = \sigma_E / E \cdot 100\%$). Figure 12 shows the results of energy reconstruction for the same experimental series. The dependence of a mean residual of the 511 keV peak $E_{\mathrm{reco}} - E_{\mathrm{ref}}$ on the source position shows that both methods perform satisfactorily, although the ELAR results seem to be free from the position dependence observed for the ELA model. In both cases, the mean residual is much smaller than the energy resolution.

2021 JINST 16 P11006

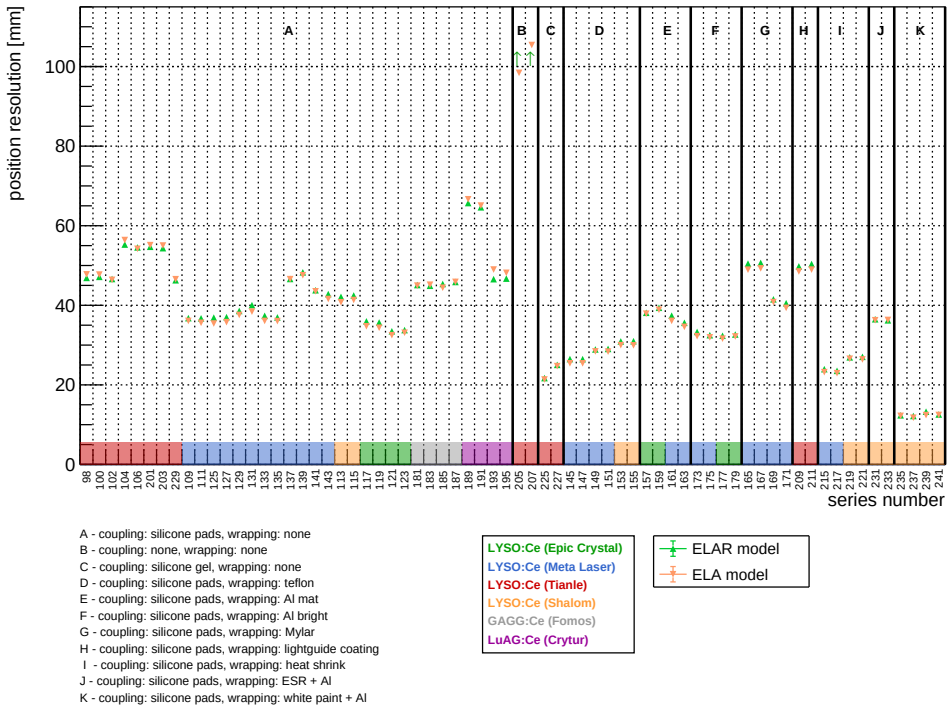

Figure 10. Position resolution determined using ELAR model and the M_{LR} method of ELA model for all analyzed measurement series. Position resolutions determined with the ELAR model for series 205 and 207 were too large to fit in the graph and were denoted with arrows. Values of position resolution for those series were in the order of 2×10^3 mm with uncertainties of 80–90 %. This is connected with the large attenuation length obtained for those series (see figure 8).

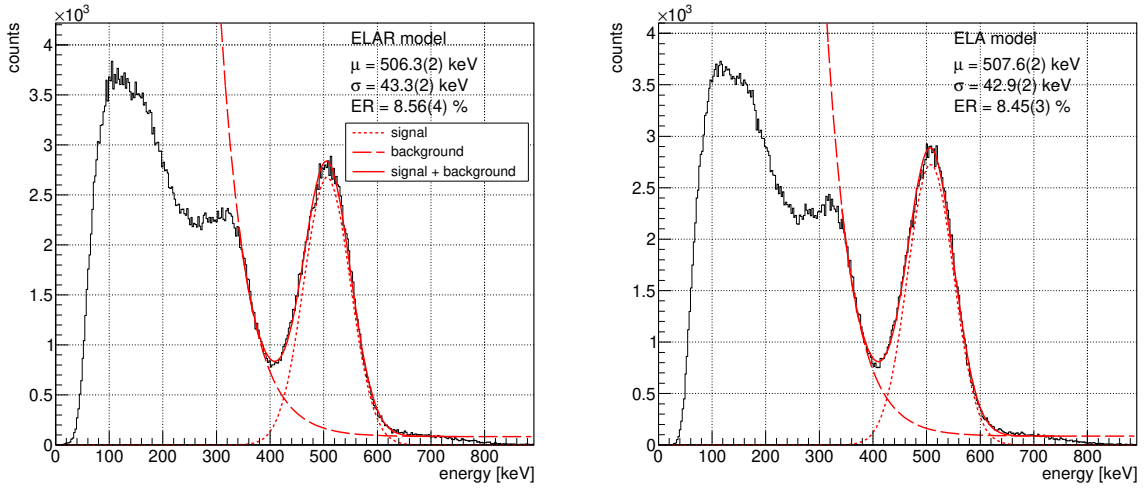

Figure 11. Example of summed energy spectra reconstructed with the two methods: within the ELAR model (left) and within the ELA model (right). Both spectra were fitted as described in section 2.4 to determine the 511 keV peak parameters and calculate the energy resolution. Presented data comes from the series 109.

2021 JINST 16 P11006

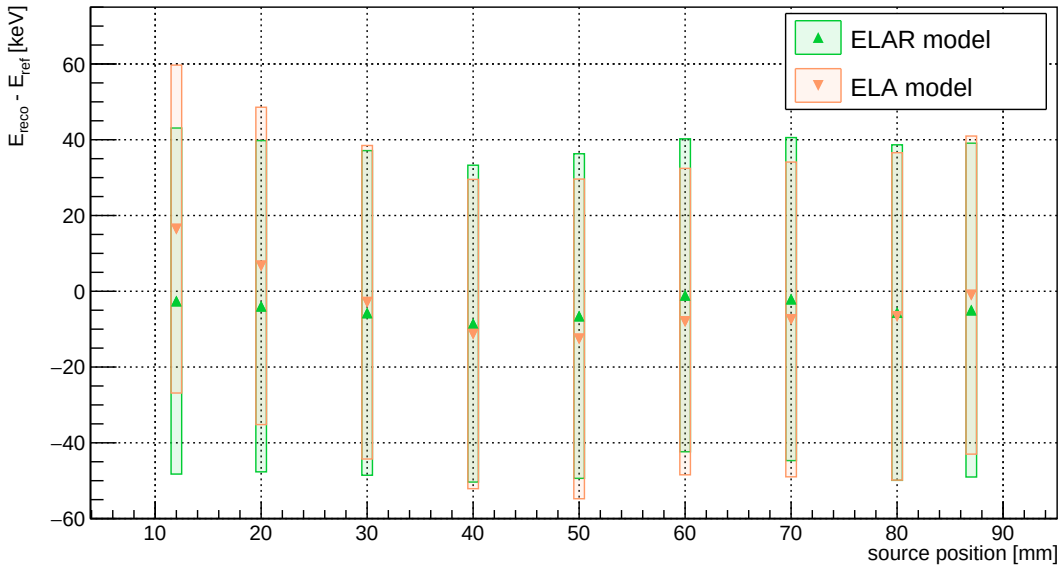

Figure 12. Residuals of energy reconstruction at 511 keV from the ELAR and the ELA models for a chosen measurement series. Error bars represent position-dependent energy resolution $\sigma(E)$ at 511 keV. Presented data comes from the series 109.

To compare the energy resolution of investigated samples, the values obtained with the two methods described above were plotted for all recorded series in figure 13. Each value was determined based on the summed reconstructed energy spectra. Differences which can be observed for different materials, couplings and wrappings are discussed further in section 5. The two methods of energy reconstruction yield very similar results as regards the energy resolution. A significant difference is visible only for fibers wrapped in ESR+Al, and those painted with the $BaSO_4$-based paint+Al.

4.5 Timing resolution

The timing resolution was determined from the time difference spectrum $T_D = t_{0,L} - t_{0,R}$ of the correlated signals recorded on both sides of the fiber, assuming that both SiPMs have comparable intrinsic timing resolution. Only events forming the 511 keV peak were included in the analysis. The obtained T_D distributions were described with the Gaussian function, whose mean μ was associated with the average time difference of signals from both ends. The timing resolution was determined as the standard deviation σ of that distribution. The mean timing resolution for the investigated fiber was calculated as a weighted mean of all measurements in the series.

Figure 14 presents an example of the μ_{T_D} dependence on the source position along the LYSO:Ce fiber. Vertical error bars represent the obtained timing resolution. Clearly, the achieved timing resolution is insufficient to reconstruct interaction position based on the t_0 time difference. The position resolution for LYSO:Ce derived from the average timing resolution is much worse than position resolution derived from charge sharing between the two ends of the fiber and yields a close-to-zero position sensitivity. Figure 15 presents the determined timing resolution values for all analyzed measurement series.

2021 JINST 16 P11006

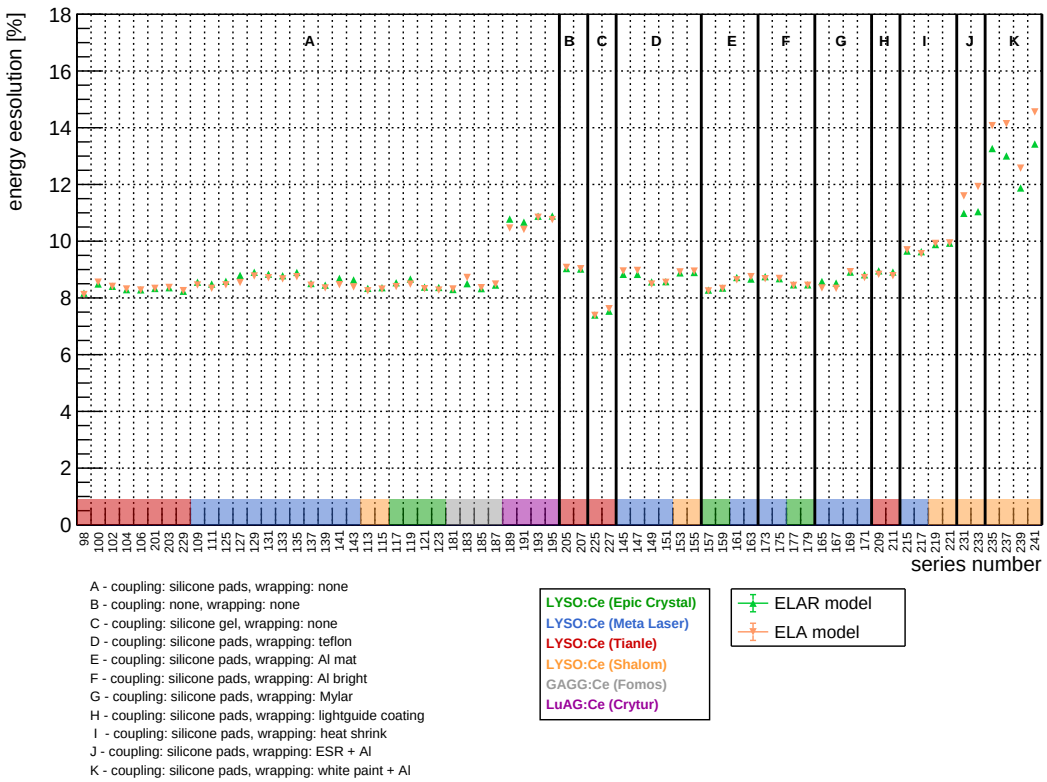

Figure 13. Energy resolution determined using both ELA and ELAR method for all analyzed measurement series.

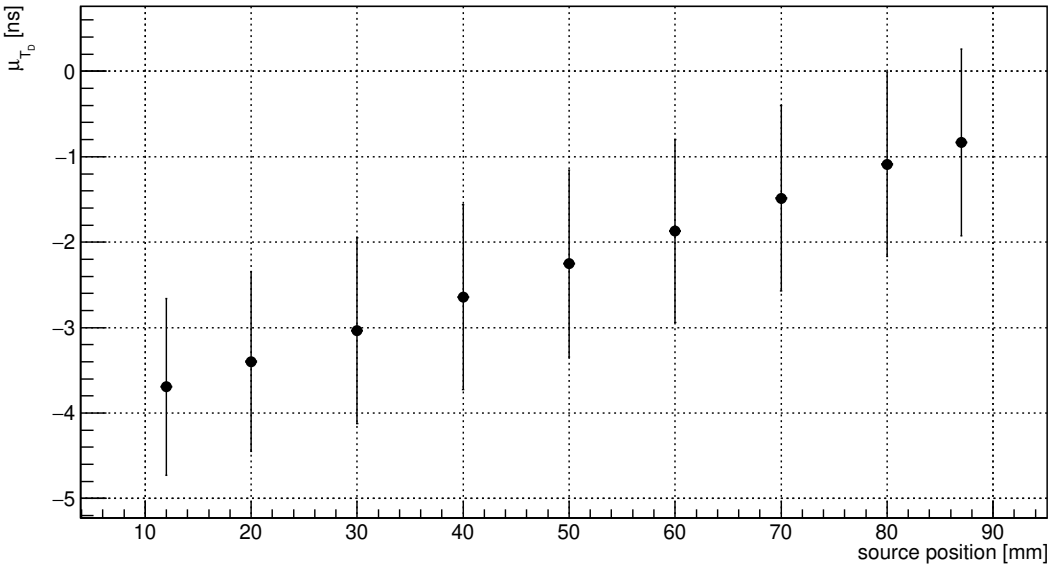

Figure 14. Dependence of the μ_{T_D} on the source position for the series 109. Vertical error bars represent the timing resolution (expressed as σ of the T_D distribution) of a given measurement.

2021 JINST 16 P11006

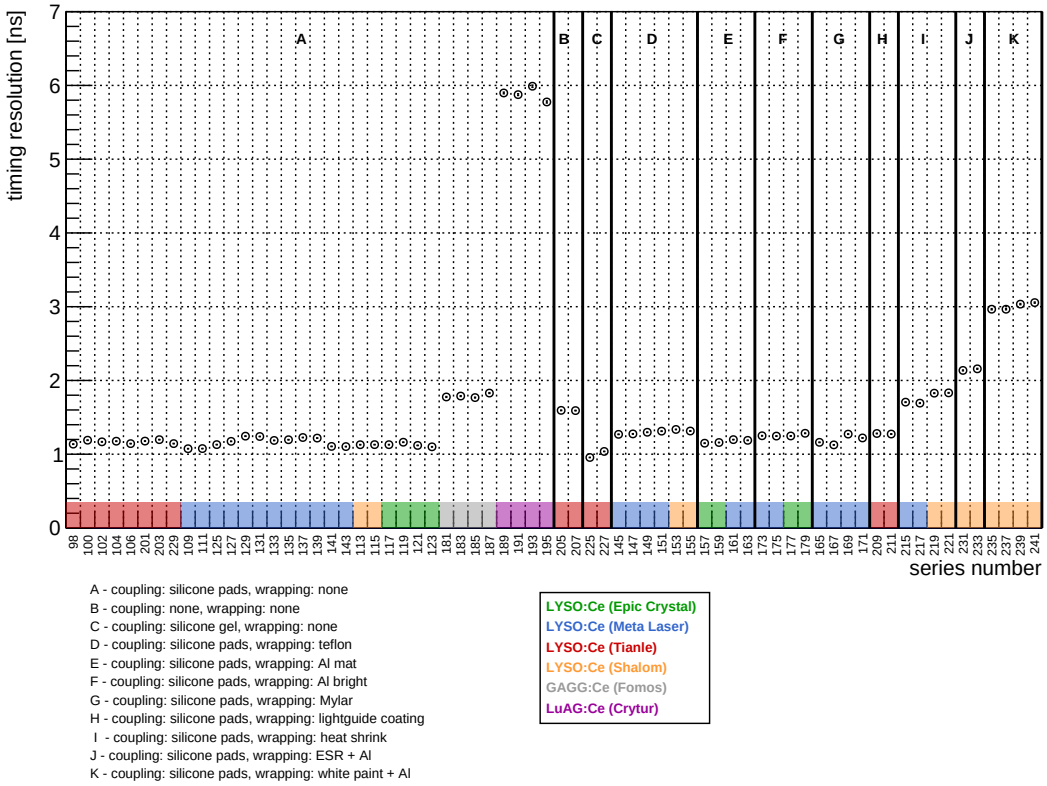

Figure 15. Obtained timing resolution for all analyzed measurement series.

It can be observed that timing resolution depends on the scintillating material, coupling, as well as the types of coating and wrapping. Those differences are further discussed in section 5.

4.6 Light collection

One of the quantities often used to describe the performance of scintillating materials is the light output, i.e. the amount of light that is produced in the place of the interaction by a 1 MeV deposit. The light output is corrected for the attenuation of scintillating light, light losses in the coupling, photodetection efficiency and cross talk probability of the SiPM, allowing to estimate the amount of produced light based on the amount of detected light. Light output is typically used to describe the properties of scintillating materials and helps to compare them in terms of their brightness. However, the performance of the SiFi-CC detector will depend on the amount of light detected by the system rather than on the amount of light produced by the scintillators alone. Therefore, for this study a property called light collection was defined as follows:

$$n_{\mathrm{LC}} = \frac{\mu_{511\,\mathrm{keV}}}{511\,\mathrm{keV}}, \tag{4.5}$$

where $\mu_{511\,\mathrm{keV}}$ is a position of the 511 keV peak in the charge spectrum expressed in PE. Values obtained for both fiber ends are summed to get the total characteristics for the investigated sample. In contrast to the light output, light collection includes effects of the applied coupling, light attenuation and properties of the used electronics, therefore it is a more suitable variable for this study. Since the light collection is not compensated for the light losses due to attenuation, its value varies with

2021 JINST 16 P11006

the source location. Hence, to characterize the investigated fiber sample a weighted mean of all measurements in the series was calculated. Figure 16 presents light collection values for all analyzed measurement series.

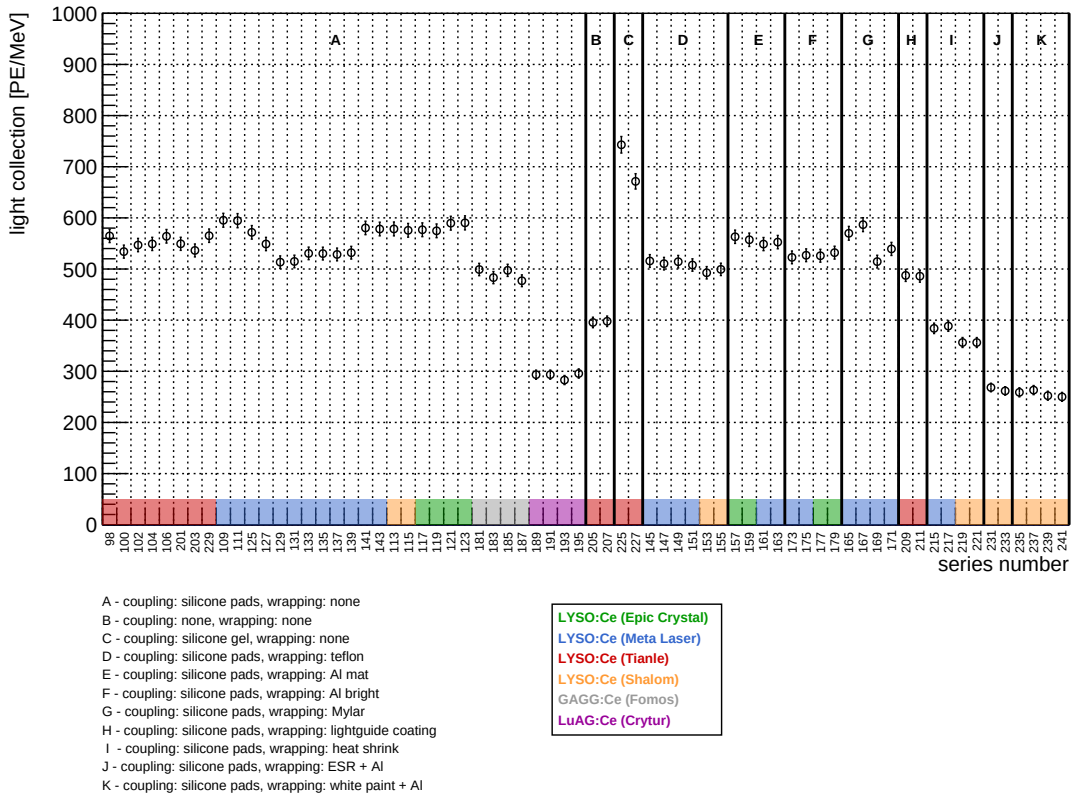

Figure 16. Values of light collection for all analyzed measurement series.

Some differences in results for different materials, types of couplings and some of the wrappings and coatings can be observed. They are discussed in detail in section 5.

5 Comparative studies

In the following section the properties of the investigated samples of scintillating fibers are compared. Comparisons are carried out for different scintillating materials, different producers of LYSO:Ce fibers, different types of fiber-SiPM coupling and different types of fiber coating and wrapping. The following properties are compared:

- Attenuation length — determined using two methods: with the M_{LR} implementation of the ELA model and with the ELAR model. Attenuation length determined using a simultaneous fit of both channels within the ELA method was not included in the comparison due to the poor quality of fits. Since it was observed that the ELAR model does not perform well for the Tianle LYSO:Ce fibers, those results were discarded in the comparative studies.

2021 JINST 16 P11006

- Position resolution — since there was no significant difference between the two described methods of position resolution determination, the method based on the M_{LR} variable within the ELA model was used in the comparative studies.
- Energy resolution — similarly as above, the ELA model and the Q_{av} variable were used.
- Timing resolution.
- Light collection.

If for a certain set of conditions several measurements were made, the presented collective result represents a weighted mean of them. There are no uncertainties listed since the calculated standard uncertainties were much smaller than the achieved measurement precision.

5.1 Different scintillating materials

Table 3 presents a comparison of properties for LYSO:Ce, GAGG:Ce and LuAG:Ce scintillating fibers. It can be seen, that all three materials are very similar in terms of the attenuation length (the difference is more pronounced for the GAGG:Ce and ELAR method). The remaining properties show, that LYSO:Ce is superior to other materials with the best values of position-, energy- and timing resolution as well as the largest light collection. GAGG:Ce, even though the obtained results are very close to LYSO:Ce, performs slightly worse in the comparison, especially in terms of timing resolution. Performance of LuAG:Ce is the worst of all three materials, with significantly worse resolutions and light collection.

It needs to be noted that timing resolution can be improved when using SiPMs of better timing properties and more elaborate electronics. In the test measurements performed with the use of Hamamatsu SiPMs (S13360-3050VE) mounted on dedicated evaluation boards (C12332-01), timing resolution below 0.5 ns was obtained (see table 3).

Table 3. Comparison of properties of different scintillating materials. Values marked with a bullet (•) were obtained in measurements with the Hamamatsu SiPMs.

Material	Attenuation length (M_{LR}) [mm]	Attenuation length (ELAR) [mm]	Position resolution [mm]	Energy resolution at 511 keV [%]	Timing resolution [ns]	Light collection [PE MeV^{-1}]
LYSO:Ce	271	121	40	8.43	1.15 0.43•	556
GAGG:Ce	278	151	45	8.47	1.79 0.58•	489
LuAG:Ce	265	116	56	10.57	5.88 2.50•	291

5.2 Different producers

Table 4 shows the comparison of the properties of LYSO:Ce fibers produced by different manufacturers. The biggest differences are visible in the attenuation length and thus also in the position resolution.

2021 JINST 16 P11006

The fibers delivered by the Epic Crystal company are characterized by the smallest attenuation length and position resolution, while the fibers produced by Tianle have the largest attenuation length and position resolution. The remaining properties are relatively similar for all manufacturers. Occurrence of big differences in attenuation length and position resolution values, while other characteristics remain comparable, can be explained by different manufacturing methods and crystal treatment. In particular, the cutting and polishing techniques and precision can affect the light propagation and absorption in the fibers. Moreover, table 4 lists timing resolution obtained in the test measurements with the Hamamatsu SiPMs.

Table 4. Comparison of properties of LYSO:Ce fibers purchased from different vendors. Values marked with a bullet (•) were obtained in measurements with the Hamamatsu SiPMs.

Producer	Attenuation length (M_{LR}) [mm]	Attenuation length (ELAR) [mm]	Position resolution [mm]	Energy resolution at 511 keV [%]	Timing resolution [ns]	Light collection [PE MeV^{-1}]
Epic Crystal	235	124	34	8.37	1.13 0.37•	583
Meta Laser	262	119	38	8.52	1.16 0.46•	549
Shalom	289	174	41	8.28	1.13	577
Tianle	356	–	50	8.35	1.17	551

5.3 Different coupling types

In order to investigate the influence of coupling, measurements were conducted with the same LYSO:Ce fiber attached to the SiPMs with the use of different coupling media: silicone gel, silicone pads and air gap (no coupling). Results of the comparison are presented in table 5. It can be observed, that the coupling significantly influences the performance of the detection system. The fiber coupled to the SiPMs with the silicone gel showed the best properties: reduced attenuation length resulting in good position resolution and large light collection leading to small energy resolution. Coupling with the use of silicone pads leads to an increase of the attenuation length and the reduction of the light collection, which result in worse position- and energy resolution. The timing resolution for both types of coupling is similar. Lack of any coupling medium between the investigated fiber and SiPMs causes a significant deterioration of the system properties: a large attenuation length results in the position resolution exceeding the length of the fiber itself. The light collection, energy- and timing resolution are also significantly worse in comparison to the previous coupling types.

The observed large differences in attenuation length can be explained by changes in collection angles caused by different types of coupling, which was previously described in [6]. Here not only optical properties of the coupling matter, but also its thickness. The thin layer of silicone gel ($d_{gel} \approx 0.4$ mm) increases the collection angle allowing to detect light leaving the fiber at a wide range of angles. Even a slightly wider air gap ($d_{air} \approx 0.6$ mm), due to the large difference of refractive indices ($n_{gel} = 1.47$, $n_{air} = 1$), decreases the collection angle, which favours light traveling straight or within a small cone. The silicone pads of a fixed 1 mm thickness due to their optical

2021 JINST 16 P11006

properties (n_{pad} = 1.43) give intermediate results. This phenomenon also explains the observed non-intuitive relation between the light collection and attenuation length.

Table 5. Comparison of properties of LYSO:Ce fiber attached to the SiPM with different types of coupling. Comparison performed for a selected Tianle fiber.

Coupling	Attenuation length (M_{LR}) [mm]	Attenuation length (ELAR) [mm]	Position resolution [mm]	Energy resolution at 511 keV [%]	Timing resolution [ns]	Light collection [PE MeV^{-1}]
Silicone gel	175	–	23	7.48	0.99	704
Silicone pad	376	–	53	8.31	1.17	552
Air gap	633	–	102	9.05	1.59	397

The above comparison shows that the silicone gel as a coupling medium can improve the performance of the scintillating detector. However, it needs to be noted that this type of coupling can be highly unstable and hard to reproduce in consecutive measurements. Therefore, this type of coupling is not suitable for certain types of experimental designs and detectors featuring scintillators. In that case, silicone pads appear to be a reasonable compromise between an optimal performance and stability and durability of the system.

5.4 Different wrappings and coatings

In many detector designs it is necessary to wrap or coat the scintillator to prevent optical cross talk between neighbouring scintillating elements or the surrounding environment. This is also the case for the SiFi-CC detection system. Besides the optical isolation, wrapping or coating modifies the fiber surface and consequently light propagation properties. For that reason, the influence of different types of coatings and wrappings were investigated. Measurements were carried out with samples of bare fibers, which were subsequently wrapped or coated with chosen materials and re-examined. The exception are fibers wrapped in ESR+Al and those painted with the $BaSO_4$-based white paint with an additional layer of Al wrapping. Those fibers were prepared by the producer, therefore it was not possible to examine them before they were wrapped and painted. The results obtained in those experimental series were compared with measurements carried out with different unwrapped and not painted samples produced by the same manufacturer (Shalom), all coupled to SiPMs via silicone pads.

Table 6 presents a comparison of the properties of bare scintillating fibers and fibers coated or wrapped with different materials. One of the proposed coatings — an AlZn spray — caused very strong attenuation of the signal in the investigated fiber, resulting in the lack of coincident signals from the fiber ends. Moreover, the obtained spectra did not feature a visible 511 keV peak, which was the basis for the data analysis, therefore they were disregarded. The influence of the remaining materials on the properties of the fibers is the following:

- Teflon: shortens the attenuation length and hence improves the position resolution. The light collection is smaller, leading to deterioration of energy resolution. Timing resolution is worse in comparison to unwrapped fibers.

2021 JINST 16 P11006

Table 6. Comparison of properties of bare LYSO:Ce fibers and fibers wrapped or coated with different materials.

Wrapping/ coating	Attenuation length (M_{LR}) [mm]	Attenuation length (ELAR) [mm]	Position resolution [mm]	Energy resolution at 511 keV [%]	Timing resolution [ns]	Light collection [PE MeV^{-1}]
Teflon	176	103	28	8.79	1.30	507
none	303	130	43	8.37	1.15	561
Mylar	303	130	44	8.55	1.19	551
none	249	119	36	8.53	1.12	559
Al (bright)	211	113	32	8.56	1.26	527
Al (mat)	254	125	37	8.47	1.17	555
none	240	122	35	8.51	1.17	548
Light guide coating	317	–	49	8.81	1.28	487
none	332	–	47	8.42	1.16	548
Heat shrink	134	83	25	9.76	1.76	371
none	303	183	44	8.34	1.17	552
ESR + Al	169	91	36	11.73	2.15	265
none	289	174	41	8.28	1.13	577
White paint + Al	46	39	12	13.85	3.01	256
none	289	174	41	8.28	1.13	577
AlZn spray	–	–	–	–	–	–

- Mylar: increases the attenuation length causing deterioration of the position resolution; the remaining properties also worsen, though less.
- Aluminum foil: depending on the wrapping method can give quite different results; if the bright side of the foil faces the investigated fiber, the attenuation length is decreased and the position resolution is improved; however, smaller light collection results in a somewhat poorer energy resolution; the timing resolution also deteriorates slightly. If the mat side of the foil faces the investigated fiber, the results are opposite, namely the attenuation length is larger and the position resolution worsens, while the light collection and energy resolution are slightly improved; the timing resolution remains unchanged. It needs to be noted that all mentioned changes in the properties are rather small in comparison to those caused by Teflon or Mylar.
- Light guide coating: the influence on attenuation length and position resolution is rather small; light collection, energy- and timing resolution all deteriorated slightly after application of the coating.
- Heat shrink: affects the investigated fibers in a way very similar to Teflon; its effect on all properties is even stronger than in the case of Teflon wrapping;

2021 JINST 16 P11006

- ESR + Al: affects the investigated fibers similarly to Teflon and heat shrink; the effect of wrapping is in particular strong for light collection, energy- and timing resolution.

- White paint + Al: affects the investigated fiber similarly to Teflon, heat shrink and ESR+Al; its effect is definitely the strongest of all listed materials; drastic shortening of the attenuation length results in excellent position resolution. However, a significant reduction of light collection causes worsening of the energy resolution. The timing resolution is also significantly poorer.

6 Summary and conclusions

In the first part of the article two models of light attenuation in the scintillating fibers were described (see section 3). The first model (ELA) assumed that the SiPMs registered light that was emitted towards them and underwent an exponential attenuation on its way through the scintillator. The second presented model, ELAR, assumed that part of the scintillating light reaching the fiber end undergoes reflection and subsequently propagates along the fiber to be registered at its opposite side. It was shown that the two implementations of the ELA model give comparable results. Although the M_{LR} is well described by a linear function of position, it does not provide a satisfactory description of the results from individual SiPMs. This may be an indication that in $S_i(x)$ there are non-exponential terms which cancel in the ratio. The ELAR method gives values of attenuation length smaller in comparison to the former two methods. This is caused by the different light propagation pattern assumed for this model. At the same time, the quality of the data description is better when compared with the ELA model, which is also reflected in χ^2/ndf values.

The energy and position were reconstructed using both ELA and ELAR methods. They gave results comparable in terms of reconstructed energy and position as well as corresponding resolutions. Therefore, it can be concluded that the straightforward methods based on the Q_{av} and M_{LR} quantities are sufficient to perform energy and position reconstruction. This is the case in particular when the detector design foresees a large number of channels, which forces the data analysis procedure to process a large number of parameters and a sophisticated uncertainties calculus. However, the ELAR method can still be used for a more detailed description of the light propagation in the scintillators.

In the second part of the article, comparative studies are presented. The following properties of scintillators were studied: attenuation length determined with the M_{LR} and ELAR methods, position-, energy- and timing- resolution and light collection. Comparisons were carried out for different scintillating materials, different manufacturers of LYSO:Ce material, different couplings as well as different fiber wrappings and coatings.

The presented systematic study allows to choose an optimal scintillating material and tune its performance for the desired experimental goal and detector design. In the case on the SiFi-CC setup, taking into account the defined requirements for the detector, the following features were chosen:

- LYSO:Ce scintillating material was chosen due to its large light collection, good timing- energy- and position resolution. This material is also relatively easy to access and affordable.

- Silicone pads were chosen as a coupling medium as a compromise between performance of the detectors and their stability and durability.

2021 JINST 16 P11006

- Al foil (bright side facing towards the fiber) was chosen as a wrapper. This material was selected since it allows to maintain a satisfactory light collection and energy resolution, while reducing slightly the light attenuation and thus improving the position resolution.

Currently, a prototype of the SiFi-CC detector module is under construction. The prototype consists of 64 LYSO:Ce fibers wrapped with the Al foil and organized in four independent layers, coupled to the SiPMs with the use of silicone pads. The prototype will allow to evaluate the collective performance of the setup, to test the technological solutions and develop necessary software tools before the full-size detector will be constructed.

Acknowledgments

This work was supported by the Polish National Science Centre (grants No. 2017/26/E/ST2/00618 and 2019/33/N/ST2/02780). We would like to thank Bogusław Kamys for many fruitful discussions and valuable comments.

References

[1] C. Dujardin, E. Auffray, E. Bourret-Courchesne, P. Dorenbos, P. Lecoq, M. Nikl et al., *Needs, trends, and advances in inorganic scintillators*, *IEEE Trans. Nucl. Sci.* **65** (2018) 1977.

[2] P. Lecoq, *Development of new scintillators for medical applications*, *Nucl. Instrum. Meth. A* **809** (2016) 130.

[3] A. Wrońska, R. Hetzel, J. Kasper, R. Lalik, A. Magiera, K. Rusiecka et al., *Characterisation of components of a scintillation-fiber-based Compton camera*, *Acta Phys. Polon. B* **51** (2020) 17.

[4] J. Kasper, K. Rusiecka, R. Hetzel, M.K. Kozani, R. Lalik, A. Magiera et al., *The SiFi-CC project — Feasibility study of a scintillation-fiber-based Compton camera for proton therapy monitoring*, *Phys. Med.* **76** (2020) 317.

[5] Crytur website, *Ionizing radiation detection — materials — LuAG:Ce*, https://www.crytur.com/materials/luagce/.

[6] K. Pauwels, C. Dujardin, S. Gundacker, K. Lebbou, P. Lecoq, M. Lucchini et al., *Single crystalline LuAG fibers for homogeneous dual-readout calorimeters*, 2013 *JINST* **8** P09019.

[7] W. Chewpraditkul, L. Swiderski, M. Moszynski, T. Szczesniak, A. Syntfeld-Kazuch, C. Wanarak et al., *Scintillation properties of LuAG:Ce, YAG:Ce and LYSO:Ce crystals for gamma-ray detection*, *IEEE Trans. Nucl. Sci.* **56** (2009) 3800.

[8] Epic Crystal website, *LYSO:Ce product description*, https://www.epic-crystal.com/oxide-scintillators/lyso-ce-scintillator.html.

[9] Meta Laser website, *Ce:LYSO scintillation detector*, https://www.meta-laser.com/scintillation-detector/ce-lyso-scintillation-detector.html.

[10] Shalom EO website, *LYSO:Ce scintillators*, https://www.shalomeo.com/Scintillators/LYSO-Ce/product-120.html.

[11] Tianle Photonics website, *Ce:LYSO Crystal*, http://www.tianlephotonics.com/product/1.

[12] I. Vilardi, A. Braem, E. Chesi, F. Ciocia, N. Colonna, F. Corsi et al., *Optimization of the effective light attenuation length of YAP:Ce and LYSO:Ce crystals for a novel geometrical PET concept*, *Nucl. Instrum. Meth. A* **564** (2006) 506.

2021 JINST 16 P11006

[13] Fomos Materials website, *Scintillation elements — GAGG:Ce*, https://en.newpiezo.com/products/scintillation_elements/.

[14] D. Dobrovolskas, G. Tamulaitis, E. Gaubas and M. Korjik, *GAGG:Ce scintillation fibers for high energy physics applications*, 2019 *JINST* **14** P06031.

[15] V.M. Kasimova, N.S. Kozlova, O.A. Buzanov and E.V. Zabelina, *Effect of Ca^{2+} and Zr^{4+} co-doping on the optical properties of $Gd_3Al_2Ga_3O_{12}$:Ce single crystals*, *Mod. Electron. Mat.* **5** (2019) 101.

[16] Y. Tamagawa, Y. Inukai, I. Ogawa and M. Kobayashi, *Alpha-gamma pulse-shape discrimination in $Gd_3Al_2Ga_3O_{12}$ (GAGG):Ce^{3+} crystal scintillator using shape indicator*, *Nucl. Instrum. Meth. A* **795** (2015) 192.

[17] B. Seitz, N. Campos Rivera and A.G. Stewart, *Energy Resolution and Temperature Dependence of Ce:GAGG Coupled to 3 mm × 3 mm Silicon Photomultipliers*, *IEEE Trans. Nucl. Sci.* **63** (2016) 503.

[18] M. Lowdon, P.G. Martin, M. Hubbard, M. Taggart, D. T. Connor, Y. Verbelen et al., *Evaluation of Scintillator Detection Materials for Application within Airborne Environmental Radiation Monitoring*, *Sensors* **19** (2019) 3828.

[19] O. Pooth, T. Radermacher, S. Weingarten and L. Weinstock, *Scintillator tiles read out with silicon photomultipliers*, 2015 *JINST* **10** T10007.

[20] P. Anfré, C. Dujardin, J.M. Fourmigué, B. Hautefeuille, K. Lebbou, C. Pédrini et al., *Evaluation of fiber-shaped LYSO for double readout gamma photon detection*, *IEEE Trans. Nucl. Sci.* **54** (2007) 391.

[21] K. Rusiecka, J. Kasper, A. Magiera, A. Stahl and A. Wrońska, *Investigation of the Properties of the Heavy Scintillating Fibers for Their Potential Use in Hadron Therapy Monitoring*, in *Engineering of Scintillation Materials and Radiation Technologies*, M. Korzhik and A. Gektin, eds., vol. 227, Springer International Publishing, 2019, pp. 195–210.

[22] R. Brun and F. Rademakers, *ROOT: An object oriented data analysis framework*, *Nucl. Instrum. Meth. A* **389** (1997) 81.

[23] K. Pauwels, M. Lucchini, A. Benaglia and E. Auffray, *Calorimeter Designs Based on Fibre-Shaped Scintillators*, in *Engineering of Scintillation Materials and Radiation Technologies*, M. Korzhik and A. Gektin, eds., vol. 200, Springer International Publishing, 2017, pp. 231–241.

[24] J. Lan, F. Zhao, M. Ding, C. Han, Y. Zhang and X. Chen, *A Universal Formula for Light Attenuation of Scintillator Detector*, *Nucl. Phys. Rew.* **36** (2019) 01.

[25] M. Taiuti, P. Rossi, R. Morandotti, M. Anghinolfi, H. Avakian, M. Battaglieri et al., *Measurement of the response of long plastic scintillator bars for the large angle electromagnetic shower calorimeter for CLAS*, *Nucl. Instrum. Meth. A* **370** (1996) 429.

[26] J. Tellinghuisen, *Statistical Error Propagation*, *J. Phys. Chem. A* **105** (2001) 3917.

[27] D.Z. Liu, Y.J. Li, J. Li, Q. Yue, H.T.K. Wong, W.C. Chang et al., *Energy reconstruction for long column CsI(Tl) crystal detector*, *Chin. Phys. C* **28** (2004) 186.

2021 JINST 16 P11006